TECHNICAL PAPER

Investigations on microstructure, crystallographic texture evolution, residual stress and mechanical properties of additive manufactured nickel-based superalloy for aerospace applications: role of industrial ageing heat treatment

Praveenkumar Vijayakumar[1] · S. Raja[2] · Maher Ali Rusho[3] · G. L. Balaji[4]

Abstract

The significant characteristics of the nickel-based Inconel 718 (IN718) superalloy are high strength, fatigue capacity, rupture strength, corrosion resistance, and creep resistance at temperatures exceeding 650 °C, which opens the application of IN718 for aircraft parts. The mechanical properties and surface residual stress (SRS) of the IN718 superalloy have been affected by fabrication and post-processing procedures, which shorten the service life of components. For the fabrication of complex aviation components, additive manufacturing of aerospace materials like IN718 has opened up new production techniques. However, localized melting and solidification produce anisotropy microstructure and a crystallographic texture with substantial tensile residual stress. These are responsible for mechanical anisotropy and pose metrological challenges for diffraction-based SRS detection. Knowing the magnitude and nature of SRS is crucial since they affect a mechanical properties and life of the parts. In this study, IN718 alloys were fabricated using the laser-based powder bed fusion (L-PBF) technique, and the impact of the standard ageing heat treatment (SAHT) process was assessed. The as-fabricated (AF) IN718 microstructure was found to have columnar dendritic structure and Laves phases in the interdendritic regions along the build direction. The SAHT sample microstructure led to the homogeneous precipitation of γ′ and γ″ strengthening phases with δ and brittle Laves phases in grain boundaries. The average grain size of 41.56 μm in AF samples was increased to 44.80 μm after SAHT. The reduction of dislocation movements resulted in converting low angle grain boundaries found in the AF sample to high angle grain boundaries. SAHT samples displayed cubical texture along the <100> and <010> directions in the (001) plane. Following SAHT, there were increases in yield and ultimate tensile strength of 26.44% and 44.74%, respectively. On the other hand, the degree of elongation decreased to 36.19%. TRS in AF samples was converted into compressive surface residual stress following SAHT due to the phase transition. The process–structure–property relationship and the impacts of SAHT on the mechanical characteristics of the IN718 produced by L-PBF have been improved upon through this study.
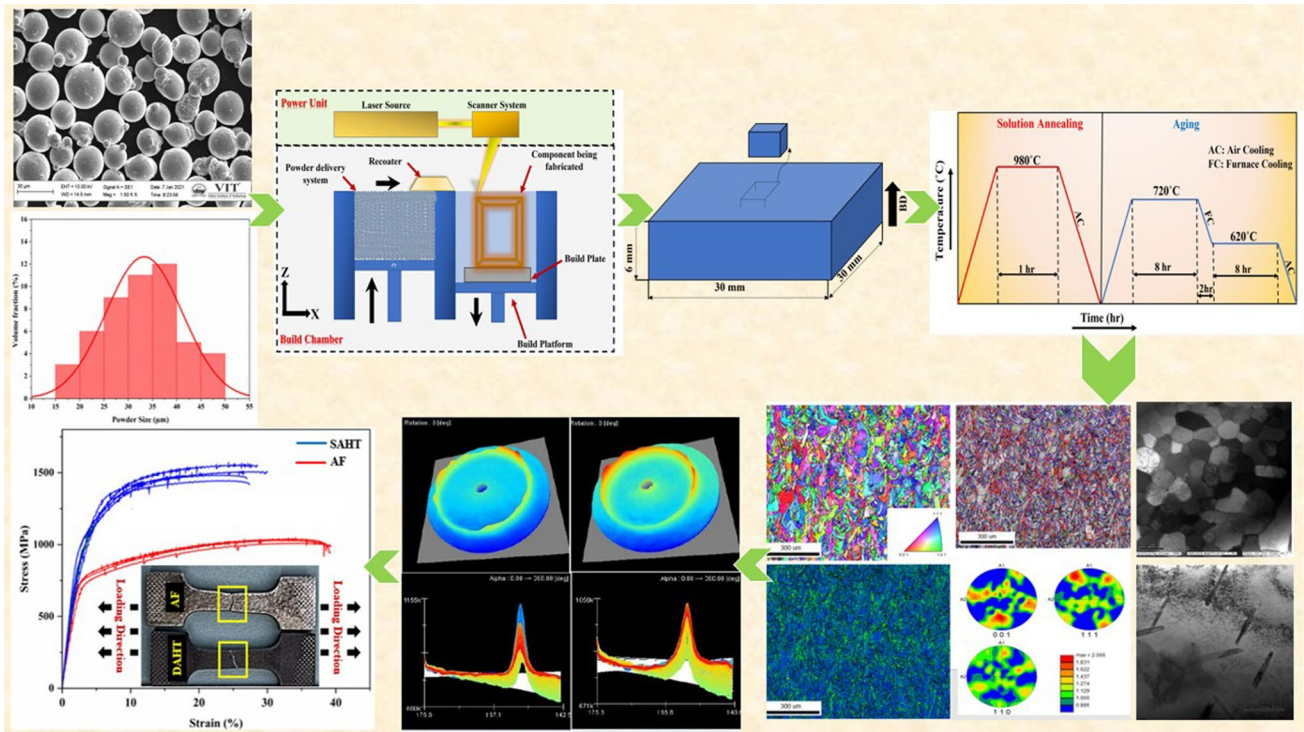
Graphical abstract

1 Introduction

Over the course of recent decades, there has been a significant increase in the utilization of elevated-temperature applications across several industries, including aerospace, petrochemical, power plant, energy, and nuclear reactor sectors [1]. The need for materials that can survive extreme circumstances throughout their use has gained significant attention in many applications. For example, the gas temperature in some areas of high-performance aircraft engines may reach up to 1090 °C [2]. Various strategies have been formulated to effectively lower the temperature of metallic components to a level that allows for the continued usage of superalloys. Inconel 718 (IN718) is recognized as a highly used superalloy because of its exceptional mechanical qualities, notable resistance to oxidation and corrosion, and ability to maintain structural integrity even when exposed to higher temperatures reaching 650 °C [3]. A significant proportion, over 50%, of the overall weight of sophisticated aviation engine components comprises the IN718 superalloy [4]. Due to

various factors, the IN718 alloy has gained widespread use in many applications, such as turbine engine components, heavily loaded rotating parts, nuclear reactors, and high-temperature bolts and fasteners [5].

Thus far, IN718 components have been manufactured by casting, wrought processes, or powder metallurgy techniques [6]. However, due to rapid advancements in turbine engine performance within the aerospace and energy sectors, intricate cooling mechanisms are consistently included in IN718 components [7]. This enhances their capacity to endure substantial temperature elevations inside sophisticated turbine engines. For example, turbine blades have been modified to include more internal cooling channels [8]. Including design and cooling elements in components leads to an escalation in fabrication costs and an increase in geometrical complexity. Furthermore, in some instances, integrating these characteristics into the manufacturing process using conventional techniques becomes unfeasible [9]. Moreover, the production of IN718 components using traditional techniques might present difficulties arising from impurity blending, elemental

segregation, and limited material removal rates during machining at ambient temperatures. There is a growing need for innovative manufacturing techniques to produce complex components of IN718, such as small nozzles used in liquid rocket engine injectors or turbine blades that include internal cooling channels [10].

The advantages of AM include waste reduction, shorter manufacturing lead times, increased flexibility, the ability to produce complex geometric products, and a shorter product development cycle [11]. The aerospace industry is one of the sectors where additive manufacturing (AM) may be used. Prominent companies such as Airbus, Boeing, NASA, and Lockheed Martin are investing substantially in advancing this technology [12]. One intriguing prospect is enhancing the buy-to-fly (BTF) ratio, which denotes the proportion between the mass of raw material required for a specific manufacturing and the ultimate mass of the fabricated component [13]. Presently, conventional manufacturing (CM) techniques yield a BTF (buy-to-fly) ratio within the range of 12:1–25:1 for aviation components, leading to a significant decline in material efficiency [12, 14]. Consequently, there is a growing emphasis on additive manufacturing (AM) processes as viable alternatives for fabricating IN718 components with minimum materials wastage, particularly within the aerospace sectors [15].

Laser powder bed fusion (LPBF) is a prominent metal additive manufacturing (AM) technique that offers significant potential for producing high-performance and intricately designed IN718 components [11]. The L-PBF technique involves localized melting of powder particles using a laser to build up a body layer by layer gradually [16]. Nevertheless, applying localized heat inputs leads to significant local temperature gradients, ultimately causing substantial internal residual stress (RS) throughout the manufacturing process [17]. Accumulating RS can result in delamination or cracking in the manufacturing process. During the cooling process, these inherent stresses contribute to the development of locked-in RS inside the final component [18]. If not adequately considered, these surface residual stresses (SRS) negatively impact the structural integrity, leading to failures in the parts over their service life [19]. Hence, it is crucial to comprehensively comprehend the influence of SRS on the efficacy of additive manufacturing components to capitalize on these prospective enhancements [20]. Further, epitaxial grain development and heterogeneous microstructure have been linked to anisotropic behaviour in laser-based powder bed fusion (L-PBF)-processed products [21, 22]. Due to the absence of fusion and the existence of gases entrapped in the powder particles, it was observed that pores formed in the L-PBF samples [23, 24]. Despite these limitations, additive manufacturing (AM) can potentially enhance the development of lightweight structures, particularly in aeronautical engineering [25].

To eliminate the microstructural anisotropy, provide a uniform microstructure, and better mechanical properties with minimum SRS, post-heat treatment (HT) is required [26]. Because of the precipitation of strengthening phases (γ' and γ'') during the HT process, the microstructure is modified, significantly impacting the characteristics. Any modification of microstructure may lead to differences in the SRS seen in the fabricated IN718 superalloy [27]. However, it has been shown that using inadequate heat treatment settings might result in the preservation of some of the harmful phases, such as the Laves phase, which could negatively affect the mechanical behaviour of LPBF IN718 [28, 29]. As a result, strong mechanical properties at high temperatures and a homogenized microstructure need appropriate post-treatments. After homogenization at 760 °C, Chlebus et al. [30] found that the Lave phases and microsegregation had disappeared [31]. The Laves phases were found to be significantly removed with the precipitation of strengthening γ' and γ'' phases in the austenite matrix when the alloy IN718 was subjected to ageing HT between 600 and 900 °C [32]. Extreme heat, between 1110 and 1250 °C, was utilized by Tucho et al. [33] to dissolve the Laves phases fully. Annealing at 1000 °C, 1100 °C, and 1200 °C was reported by Dinda et al. [34] to entirely transform the grain structures from columnar to totally homogenized equiaxed structures. The HT of IN718 alloy between 980 and 1200 °C, as described by Calandri et al. [35], enhances hardness through the precipitation of strengthening γ'' phases. The study conducted by Sochalski-Kolbus et al. [36] revealed that the production of Laves phases significantly contributes to the development of RS. This is attributed to variations in crystallographic structures and orientations in relation to the primary γ phase, which in turn alters the lattice spacing that is free from stress. The eutectic transition is responsible for non-equilibrium solidification in cases when the elements of Nb, Ti, and Mo become more concentrated in the liquid metal. This process is followed by volumetric shrinkage, leading to the production of significant dislocation and SRS [37].

The solid solution annealing followed by ageing in an HT is the fundamental process by which the characteristics and SRS of IN718 alloy [38]. It was found that improving the metallurgical, mechanical characteristics and mitigation of SRS of alloy IN718 requires eliminating undesirable phases from the microstructure by appropriate heat treatment. However, the mechanical behaviour of LPBF IN718 was not wholly explained since homogenization and solution affected the phases, texture and SRS differently. However, the effect of microstructural changes on mechanical properties and the changes in residual stress after heat treatment were limitedly addressed in the literature.

The structure–property-SRS correlation has been made which is the primary novelty of the present work. To the best of author's knowledge, most of the published work
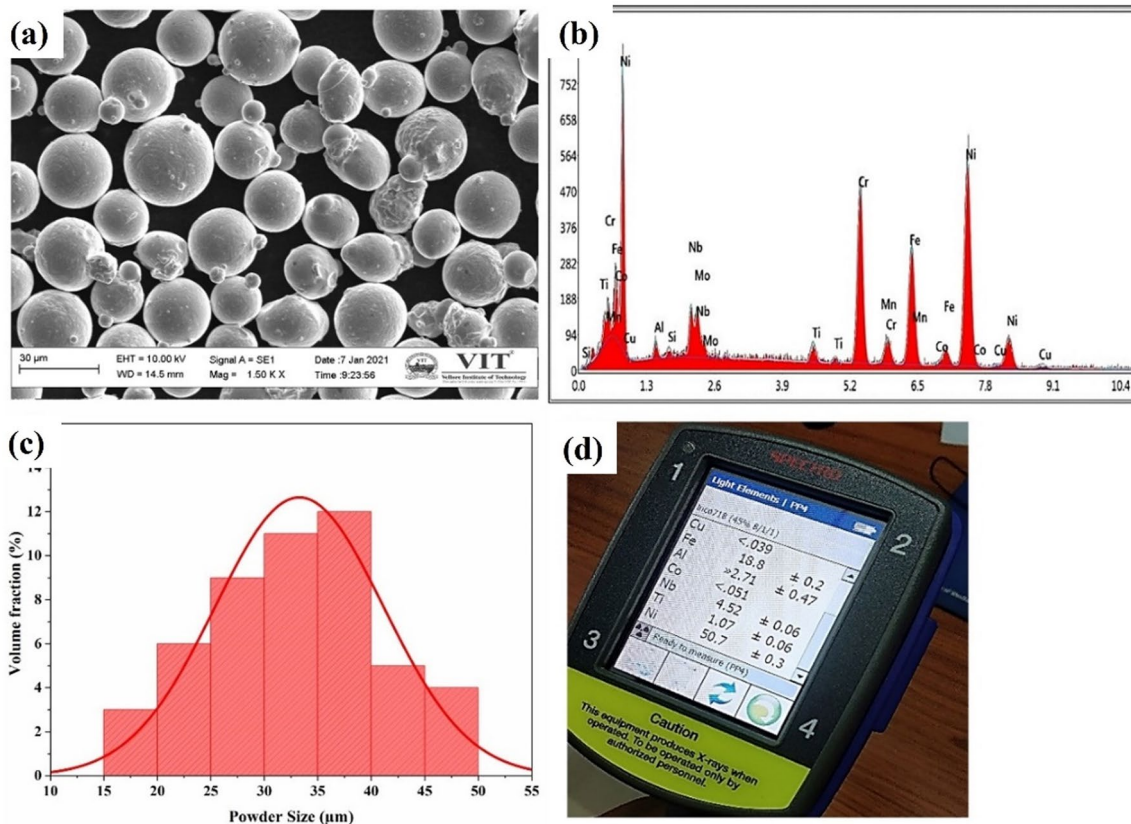
Fig. 1 IN718 powder characterization: **a** Morphology of powder particles, **b** EDS spectrum of powder particles, **c** IN718 Powder particles size distribution, **d** elemental analysis using handheld portable XRF

Table 1 EOS IN718 powder physical properties

Powder	Apparent density (g/cm^3)	True density (g/cm^3)	Particle size range (μm)	Hall flowrate [s (50 g)$^{-1}$]	Tap density (g/cm^3)
EOS IN718 powder	3.889	8.23	5–53	29.34±0.32	4.1383 (for 3000 taps)

Table 2 Elemental composition of IN718 powder in wt%

Elements		Ni	Cr	Mo	Nb	Co	C	Mn	Si	S	Cu	Al	Ti	Fe
Weight %	Powder	52.1	19.4	3.21	5.13	0.27	0.06	0.052	0.046	0.01	0.032	0.31	0.90	19.0
AMS5662	Min	50	17	2.80	4.75	–	–	–	–	–	–	0.20	0.65	Bal
	Max	55	21	3.30	5.50	1.00	0.08	0.35	0.35	0.015	0.30	0.80	1.15	

concentrated only on the microstructural changes after ageing. The SRS analysis of L-PBF components after fabrication ageing thermal treatment methods has only seen limited use in the available literature. The current study seeks to connect the structure–property relationship and SRS on IN718 alloy manufactured by the L-PBF technique to achieve high mechanical characteristics, strong crystallographic texture orientation with minimum SRS for aerospace applications through standard ageing heat treatment (SAHT). This research also intends to differentiate local alterations in L-PBF IN718 superalloy SRS, microstructure, crystallographic texture orientation and mechanical properties before and after SAHT.

Fig. 2 Schematic and L-PBF fabricated IN718 metal blocks in powder bed
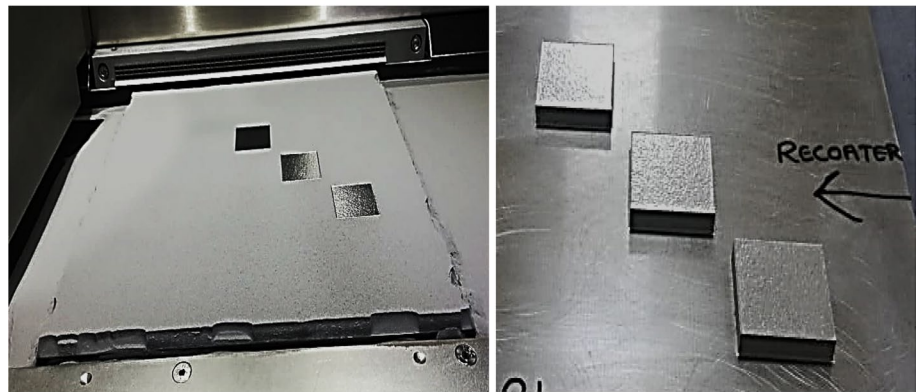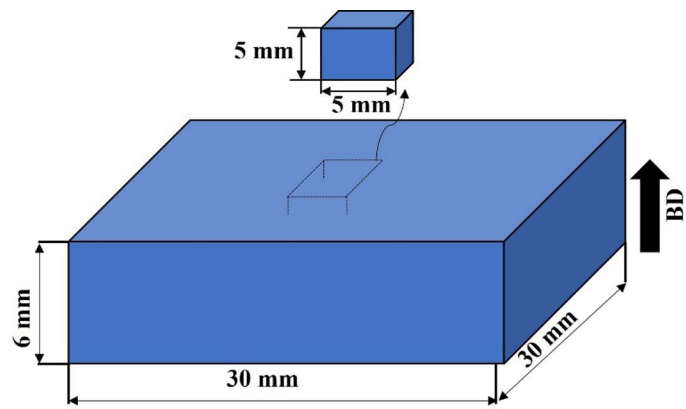
Table 3 Process parameters used for fabrication of IN718 superalloy

S No	L-PBF process parameters	
1	Laser power (W)	280
2	Scan speed (mm/sec)	960
3	Layer thickness (μm)	40
4	Laser spot size (μm)	80
5	Hatch spacing (μm)	110
6	Dwell time (Sec)	12
8	Volumetric energy density (J/mm^3)	66.3
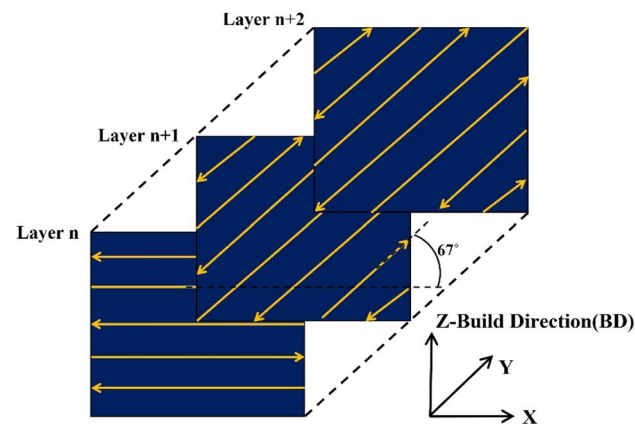
**Fig. 3** Schematic of scanning pattern followed to fabricate IN718

2 Raw materials and experimental methods

2.1 IN718 powder particles and fabrication procedure

The fresh unused gas atomized (EOS) IN718 powder particles of size ranging between 15 and 50 μm with a mean particle size of 40 μm were used for fabrication, as well as characterization of IN718 particles, as shown in Fig. 1. The scanning electron microscope (SEM) images of IN718 powder particles show that the powder particle morphologies used for fabrication are typically spherical. The physical properties of EOS IN718 powder particles are listed in Table 1. The energy-dispersive X-ray spectroscopy (EDS) analysis was carried out to distinguish the chemical composition of alloying element in the powder particles and is listed in Table 2. It shows that the wt% of alloying element in the IN718 powder particles is within the permissible range as per the standard UNS N07718 and AMS 5662.

The 3D CAD model of a metal block size 30 mm×30 mm×6 mm was designed using Solidworks design software, as shown in Fig. 2. The designed CAD files were exported to preprocessing Materialize Magics RP software in STL format to define the fabrication process parameters. The IN718 metal blocks are fabricated using the laser powder bed fusion (L-PBF) process (EOS M280) in an inert
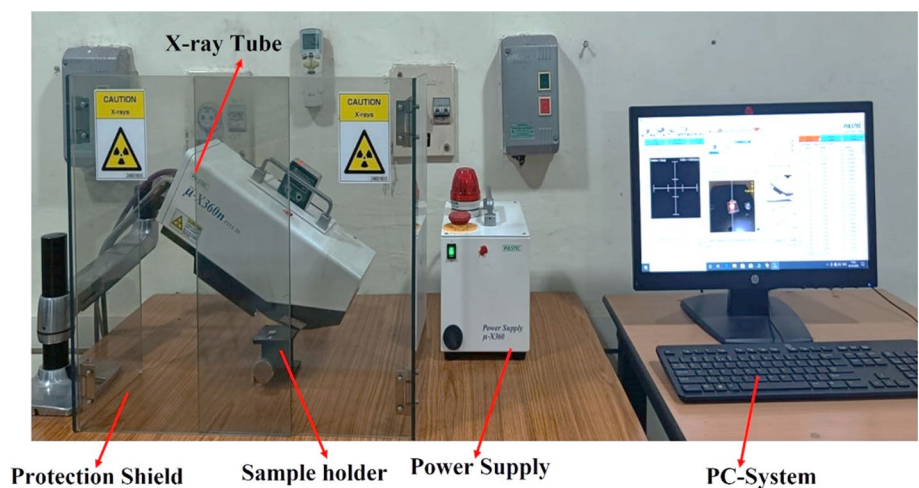
Fig. 4 Heat treatment cycle followed in SAHT
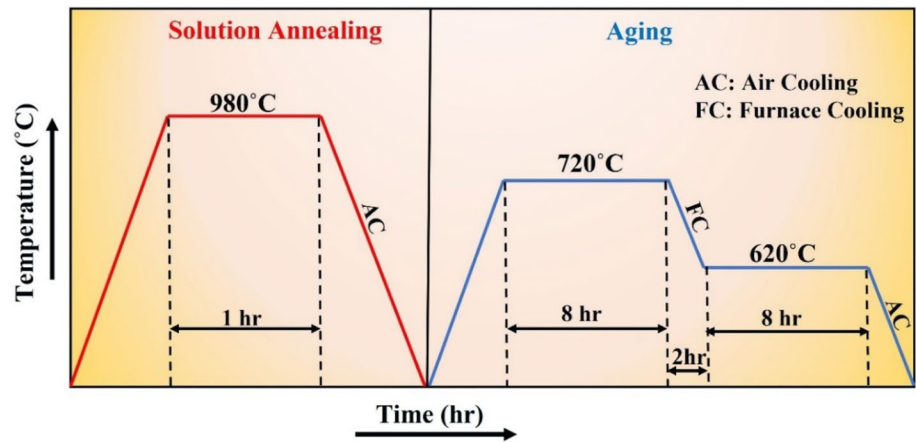
Fig. 5 Experimental tubular furnace setup for SAHT
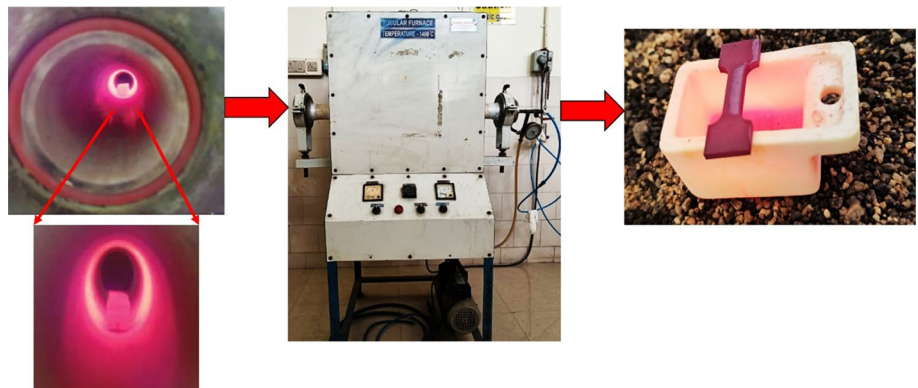

**Fig. 6** XRD-cos α RS analyser setup

environment which employs a YB fibre (ytterbium) laser to melt the powder bed. The process parameters of L-PBF machine play an important role in fabricating the defect free samples. The IN718 samples were fabricated using identified process parameters. In this research work, parameters used for fabrication of IN718 are listed in Table 3 and the fabricated IN718 metal blocks are shown in Fig. 2. The metal blocks are fabricated on the built platform, which was preheated with a temperature of 80 °C to reduce the thermal gradient (TG) between the built platform and the fabricated metal block and thermal distortions. The fabrication was done by rotating each successive layer in a build direction for 67° (rotated scanning strategy) in an antilock-wise direction, giving sufficient time to solidify and leading to an even and consistent heating and cooling cycle, reducing the TG [39].
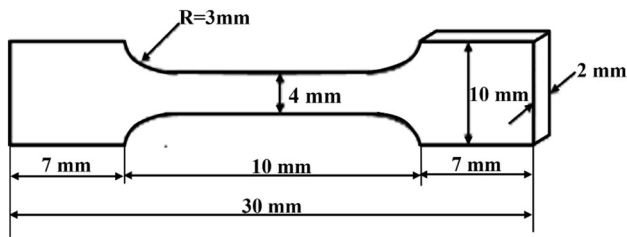
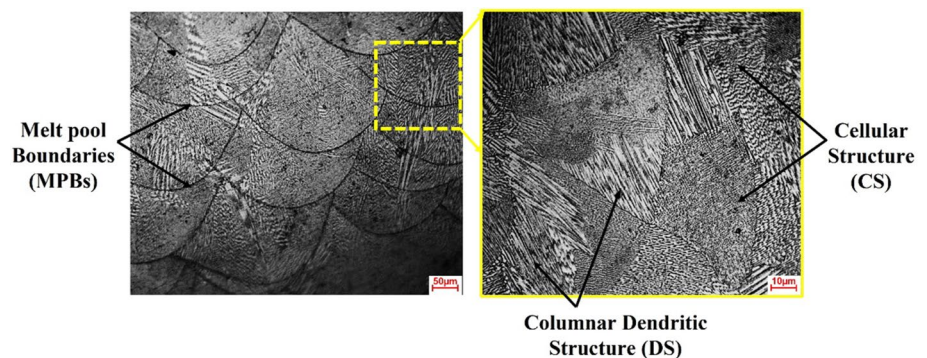**Fig. 7** Schematic of L-PBF IN718 tensile specimen as per standard ASTM-E8M
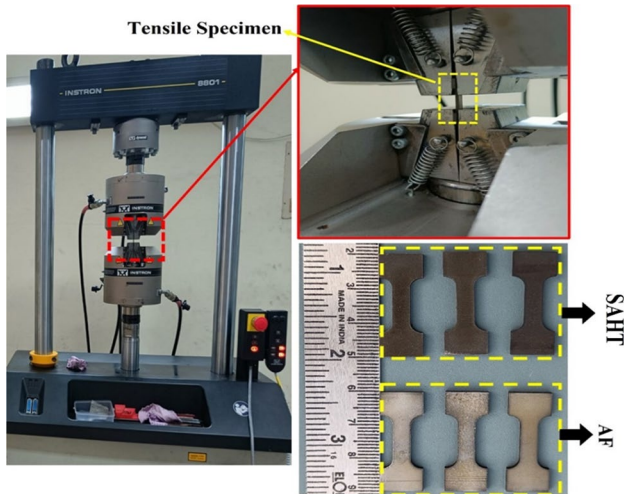
Fig. 8 Tensile testing and extracted samples of L-PBF IN718

The schematic representation of the 67° rotated scanning strategy employed in this work is shown in Fig. 3.

2.2 Heat treatment cycle

The post-standard ageing heat treatment (SAHT) was performed on the as-fabricated (AF) IN718 metal block after removed from the build platform based on the standard AMS5662 which comprises solution annealing and double ageing process. The step-by-step SAHT cycle is schematically represented in Fig. 4. The SAHT cycle encompasses solution annealing at 980 °C for 1 h followed by air cool (AC) to room temperature. After solution annealing the metal blocks were subjected to double ageing treatment: at 720 °C for 8 h followed by furnace cool (FC) at 50 °C/h to 620 °C, maintain 620 °C for 8 h and then air cool to room temperature. In this present work, heat treatment process was performed in a vacuum tubular furnace with a slow heating and cooling rate of 10 °C/min and 5 °C/min as shown in Fig. 5.

2.3 Characterization study

Two sets of small cubical of size 5 mm×5 mm×5 mm were cut and extracted from both AF and SAHT metal blocks of size 30 mm×30 mm×6 mm for characterization studies as shown in Fig. 2. The extracted cubical was polished with rough to fine-grade sand papers sequentially. After that, the cubical was laid open to disc polishing on a fine velvet cloth with alumina powder and diamond paste. Subsequently, the mirror polished cubical was etched with the manually prepared Kalling's reagent etchant for 2 s. The microstructure of the etched cubical was captured using Carl Zeiss optical microscope (OM) and FEI quanta field emission scanning electron microscope (FE-SEM). The alloying elements and precipitations were quantified using energy-dispersive X-ray spectroscopy (EDS) attached to the FE-SEM setup. One set of both AF and SAHT cubical was electro-polished with an electrolyte of methanol and perchloric acid (80:20) for crystallographic texture analysis using an electron-backscatter diffraction (EBSD) setup. The FEI Quanta EBSD setup was operating at 30 kV and 50 mA. The cubical was analysed with a step size and tilt angle of 0.4 and 70°, respectively.

2.4 Surface residual stress study

The SRS accumulated on the AF and SAHT metal blocks was measured using Pulstec μ-360 X-ray diffraction (XRD)

Fig. 9 Optical microstructure results of AF IN718

stress analyser. XRD stress analyser works on the principle of Bragg's law, and values are computed based on the cosα method as shown in Fig. 6. The Cr-based X-ray tube and X-ray with a wavelength of 2.29093 Å were used to measure the SRS in the nickel-based superalloy with an operating temperature between 5 and 40 °C. The diffraction plane was set as (311), and diffraction was set to 30° for nickel-based superalloy, which owns FCC crystal structure. Both the AF and SAHT metal blocks had their SRS calculated at four adjacent points on the top surface, including the corners and the centre regions within the layer. The average SRS readings were published with a margin of error. Each XRD test began with a calibration using a stress-free platinum disc and ferrite powder to ensure optimal conditions. The residual stress measurement was performed on the samples top surface on both AF and SAHT condition before cutting the samples for further characterization studies.

2.5 Mechanical characterization study

The schematic representation of tensile samples with dimensions as per the standard ASTM E8 is shown in Fig. 7. Figure 8 shows that three sets of the miniature tensile sample per the standard ASTM E8 were cut and extracted from both AF and SAHT metal blocks. The strain rate for this test was 0.5 mm/min, and it was conducted using a Instron universal testing machine (UTM).

3 Results and discussion

3.1 Microstructural study

3.1.1 Optical, SEM, TEM and EDS analysis

The microstructure of the IN718 superalloy formed after L-PBF fabrication results from a non-equilibrium, directional solidification due to differences in temperature, fast rate of cooling, and repeated layer remelting. The optical images of the AF IN718 superalloy are shown in Fig. 9. It shows arc-shaped melt pool boundaries (MPBs) due to the Gaussian energy distribution of the laser along the build direction. The MPBs are arranged hierarchically due to the overlap of laser tracks and the remelting of layers along the build direction. The average width and depth of the as-built MPBs are measured, ranging between ~ 120 and ~ 140 μm. Further, the higher magnification of optical microstructural images revealed the presence of randomly oriented fine columnar dendritic structure (DS) and cellular structure (CS) within the MPBs and crossing several MPBs. The presence of both DS and CS resulted in a microstructural anisotropy. The anisotropy refers to the non-uniform distribution of microscopic features within a material, such as grains, phases, or defects, in different directions [3]. This anisotropy can arise due to various factors like processing condition, and growth mechanisms, resulting in directional variations in material properties [5]. In L-PBF, it often manifests as differences in grain orientation, size, grain growth direction and distribution within the AF IN718 samples.

The SEM images of the as-built microstructure confirmed the formation and presence of DS and CS and crossed several MPBs. The DS tends to grow in the heat flow direction from the top to the bottom of the melt pool. It is evident that the high TG is predominant along the build direction and also due to the Marangoni flow of the melt pool. The remelting zone is formed due to remelting of layers as well as the overlapping of neighbour layer tracks and MPBs, as shown in Fig. 10. The coarser CS are distributed on the remelting zone and interface of MPBs. It is mainly due to the temperature difference between the newly melted and remelted regions. Both optical and SEM images do not show any defects due to the use of optimized process parameters for fabricating the IN718 superalloy. The point EDS analysis represented in Fig. 10, shows that the heterogeneity in the elemental microsegregation at the basic γ matrix (dendritic regions) and interdendritic regions. From the point EDS analysis, it was observed that positive Nb segregation in both dendritic and interdendritic regions of DS and CS. The wt % of Nb in interdendritic and dendritic regions of DS are 9.7% and 4.7%, similar for CS are 10.1% and 4.8%. It was observed that the Nb segregation was higher in the interdendritic regions than in the dendritic regions in both DS and CS. This is mainly due to the high cooling rate (10^3–10^5 K/s) of the L-PBF process [40]. The high cooling rate does not give sufficient time to solute the Nb elements in the matrix. Also, the shorter time it takes for the liquid pool to solidify makes it easier to trap Nb in the spaces between the dendrites (interdendritic regions), which primes to the creation of the Laves phase [(Ni, Fe, Cr)$_2$ (Nb, Mo, Ti)]. The formation of irregular block-shaped Laves phase in the interdendritic regions of DS is evident in the SEM micrographs AF IN718 superalloy, as shown in Fig. 10. The TEM images of the AF IN718 superalloy disclosed a high density of dislocations due to repeated multiple heating and cooling cycles. The dislocations were clearly visible in TEM images of the AF condition, as shown in Fig. 11a. The repeated thermal cycles caused heterogeneous CR rates and heterogeneous TG rates for each layer, resulting in a high density of dislocations [41]. TEM clearly identified the presence of an irregular-shaped Laves phase, as shown in Fig. 11b.

As can be seen in Fig. 12, optical examinations of the SAHT microstructure demonstrate that all traces of the
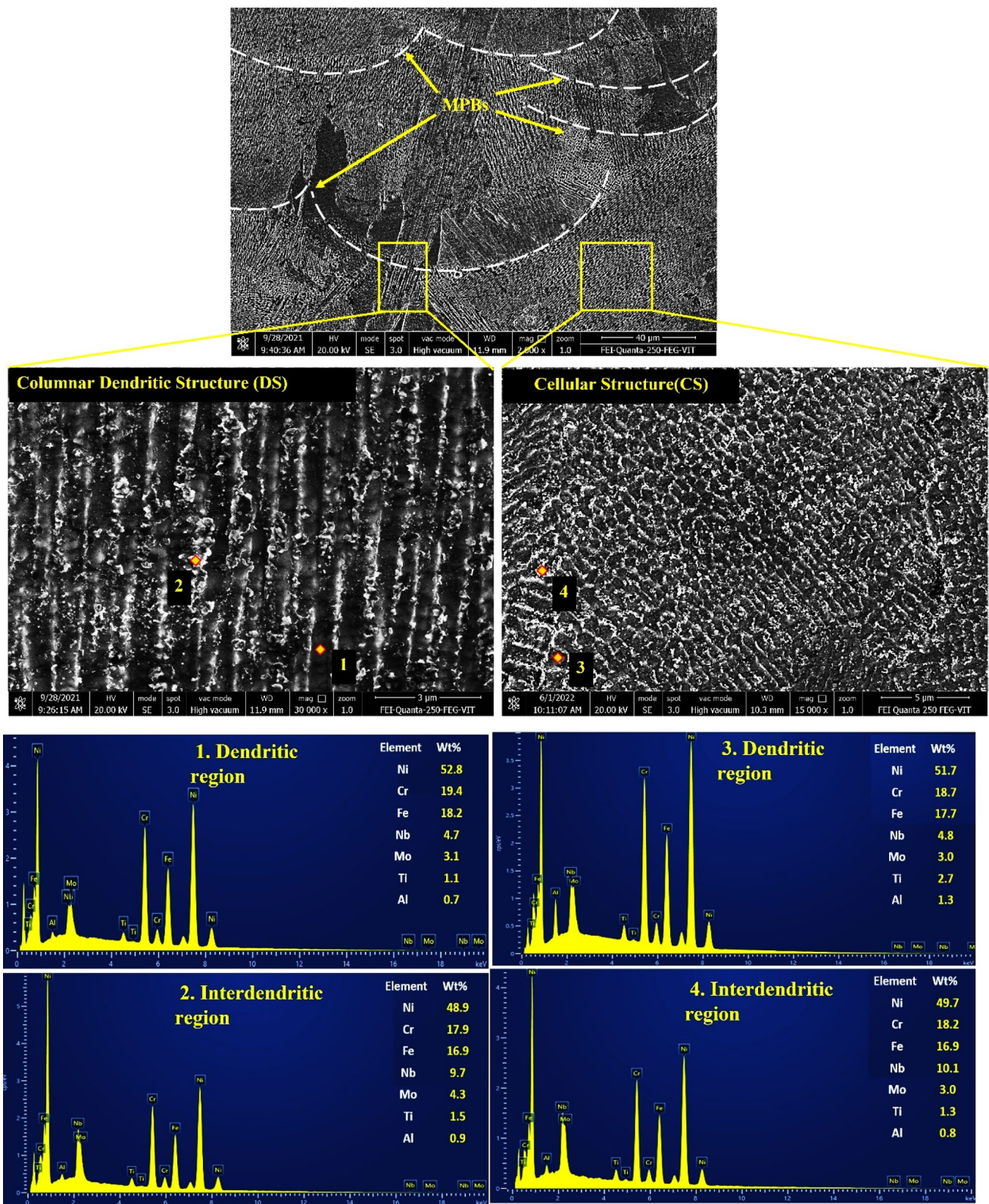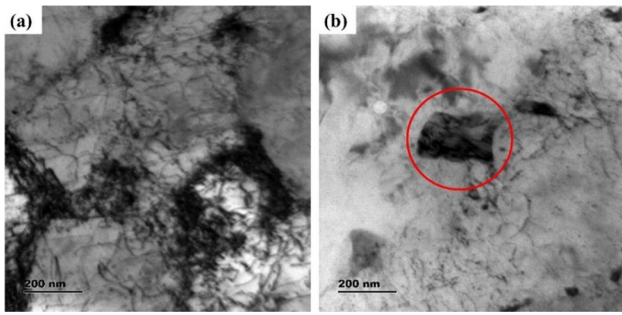
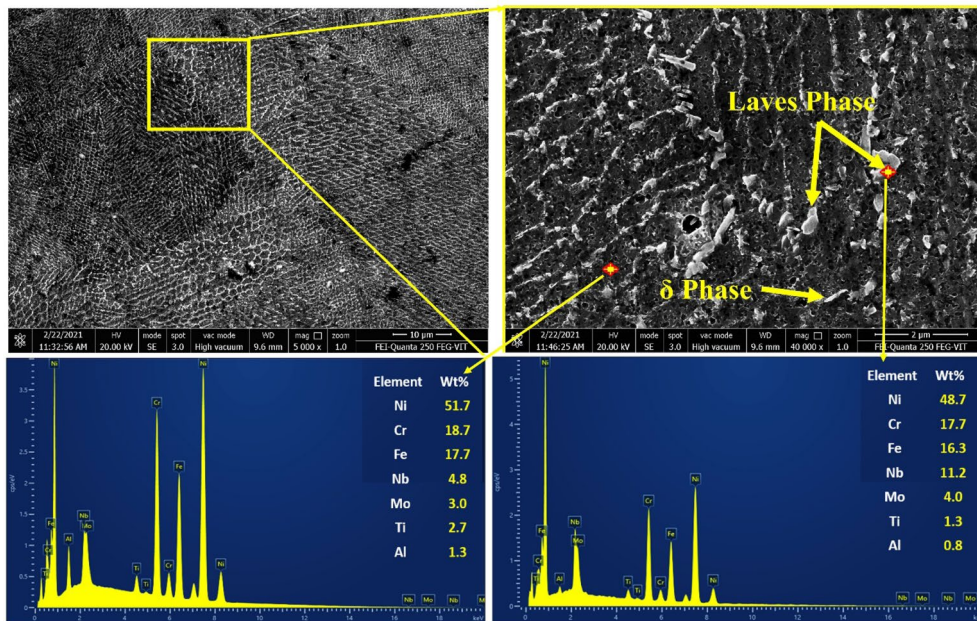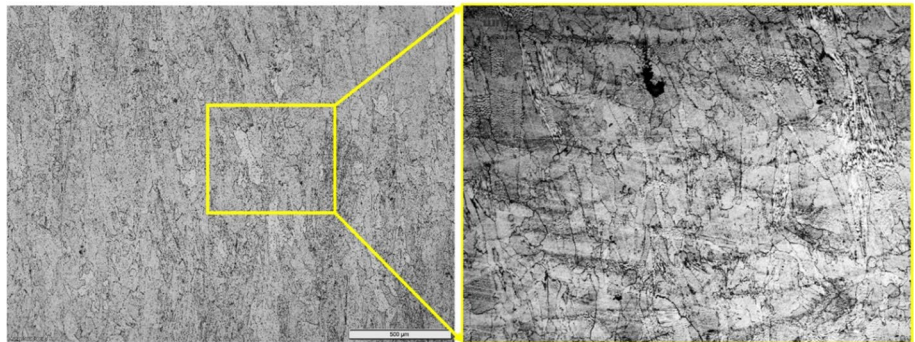**Fig. 10** SEM and EDS results of AF IN718

Fig. 11 TEM results of AF IN718 representing **a** dislocation density, **b** Laves phases

melt pools have been dissolved and disappeared. Recrystallization and restoration of the grain morphology were

shown to be successfully introduced using SAHT. Figure 13 displays the SEM microstructures of SAHT IN718 samples, the arrows point to areas where needle-like δ phase and disc-shaped Laves phases precipitated in the grain boundaries, also indicating the disappearance of the columnar dendrites. At high temperatures, the Nb-rich Laves phases were dissolved in the matrix, leading to the nucleation of additional γ'' phases inside the grains. EDS analysis indicated that the partial dissolution of Laves phases resulted in the release of additional Nb and Ti, which subsequently interacted with the basic γ matrix to generate the stronger γ'' (Ni3Nb) phase. The EDS analysis in Fig. 13 confirms that the lower solution annealing temperature (980 °C) than the melting temperature of Laves phase (1165 °C) led to the precipitation of Laves phases in the grain boundaries.

Fig. 12 Optical microstructure results of SAHT IN718

Fig. 13 SEM and EDS results of SAHT IN718
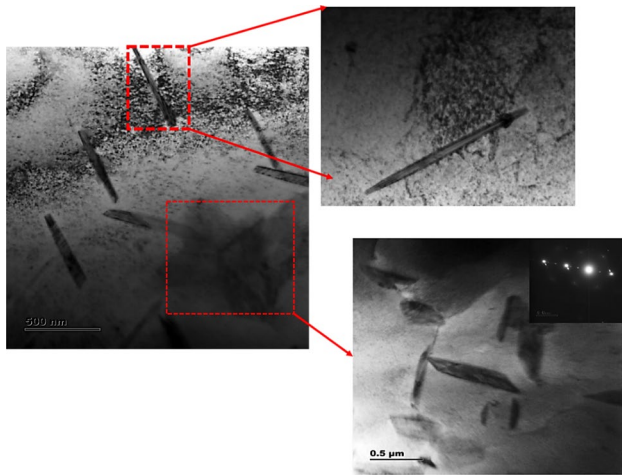
Fig. 14 TEM observation of SAHT IN718

As can be seen in Fig. 14, TEM observations revealed that the discontinuous δ phases were found throughout the grains and also organised at the grain boundaries. The SAHT is performed in a controlled environment, where the heating and cooling rates are very slow at the rate of 5 °C. It prevents the development of the δ phase, which begins at 780 °C and continues until 900 °C, ensuring that the γ'' phase occurs before the δ phase. Despite being more thermodynamically stable than the γ'' phases, the δ phase's sluggish precipitation kinetics cause the γ'' phases to nucleate earlier than the δ phases. Furthermore, prolonged contact durations at 980 °C diminish the volume fraction of the δ phase, and the solution heating temperature is near to the solidus temperature (990–1020 °C), which inhibits the expansion of the δ phase [42]. In most cases, the γ'' phase's intensity is reduced as a result of formation of δ phases. Despite the negative effects, grain growth was prevented because the δ phase in the grain boundaries worked as a pinning medium and prevented dislocation motion. Grain growth was interrupted when the δ phase precipitated in the boundaries at its solidus temperature of 1010 °C. Furthermore, in sites where the Nb concentration is greater than 6.8% molar percentage, the δ phase may develop and propagate [43].

3.1.2 Texture, IPF, PF and KAM map analysis

As can be seen in Fig. 15, EBSD was used to further investigate the grain morphology of the AF IN718 alloy. Directional solidification is responsible for the creation of elongated grains in the build direction in the XZ plane, as demonstrated by the IPF map in Fig. 15. It also displays an average XZ-plane grain size of 41.56 μm. A strong texture with pole intensity of 4.472 was detected in the <001> direction in the (001) plane, which displayed the material texture as pole Figs. Most grains were seen to be aligned in

a <001> orientation, which coincided with the direction of grain development and heat flow. The misorientation distribution map, which shows that a majority of low angle grain boundaries (LAGBs) of 64% have quite significant dislocation density, whereas only a minority of high angle grain boundaries (HAGBs) of 35%. This is mainly due to AF sample ability to tolerate the significant thermal strain caused on by the fast cooling. The change in colour indicative of microscopic strain is closely correlated with the dislocation density, demonstrating the significance of the Kernel average misorientation (KAM) map [44]. Stain regions (green on the KAM map) were found over the whole scanned area, and the average KAM value of AF IN718 as developed is 0.91.

The inverse pole Fig (IPF) of the SAHT sample represented in Fig. 15 clearly reveals the presence of non-uniform elongated grains along the build direction which implies that SAHT is able to activate the recrystallization and columnar grains transformed into equiaxed grains. The average grain size as 44.80 μm in the *XZ* plane and a slight increase in average grain size compared to SRHT. The pole Fig reveals the columnar texture of the as-built sample replaced with a cubical texture in <100> and <010> direction in (001) plane with reduction in pole intensity 4.472–4.165. The reduction in pole intensity after SAHT confirms the changes in grain morphology and homogenization. The misorientation distribution map of SAHT revealed a large amount (47%) of HAGBs with reduction in small amount (52%) of LAGBs. The result shows the SAHT effectively converting the LAGBs to HAGBs due to atomic rearrangement which resulted in dislocation density reduction. The KAM map showed reduction in stain region (green colour) after SAHT. The average KAM value was found to be decreased from 0.912 to 0.618, i.e. 38% indicating reduction in strain area.

3.2 XRD analysis

Figure 16 displays the X-ray diffraction (XRD) patterns obtained from powder particles, AF, and SAHT conditions. At all cases, the peaks of the basic γ (Ni–Cr–Fe) phase were seen at the (111), (200), (311), and (222) planes. The existence of the γ' (Ni_3Nb) phase was further confirmed by the peaks obtained from the XRD pattern of the powder particles and AF conditions. New peaks, including those corresponding to the γ' (Ni_3Nb), γ'' (Ni_3 (Al, Ti)), and δ ($NbNi_3$) phases, were discovered in the XRD pattern of SAHT. It also shows that δ phases are not present under AF conditions but observed under SAHT condition. The peaks of γ'' were more in the SAHT condition which was the key factor for increase in the strength of the component. Further, the size of Laves phases as compared to the basic austenite γ phase is too small which causes the peaks of the Lave phases too weak to detect. The XRD technique has size limits as the

Fig. 15 EBSD results of L-PBF IN718 alloy in both AF and SAHT condition
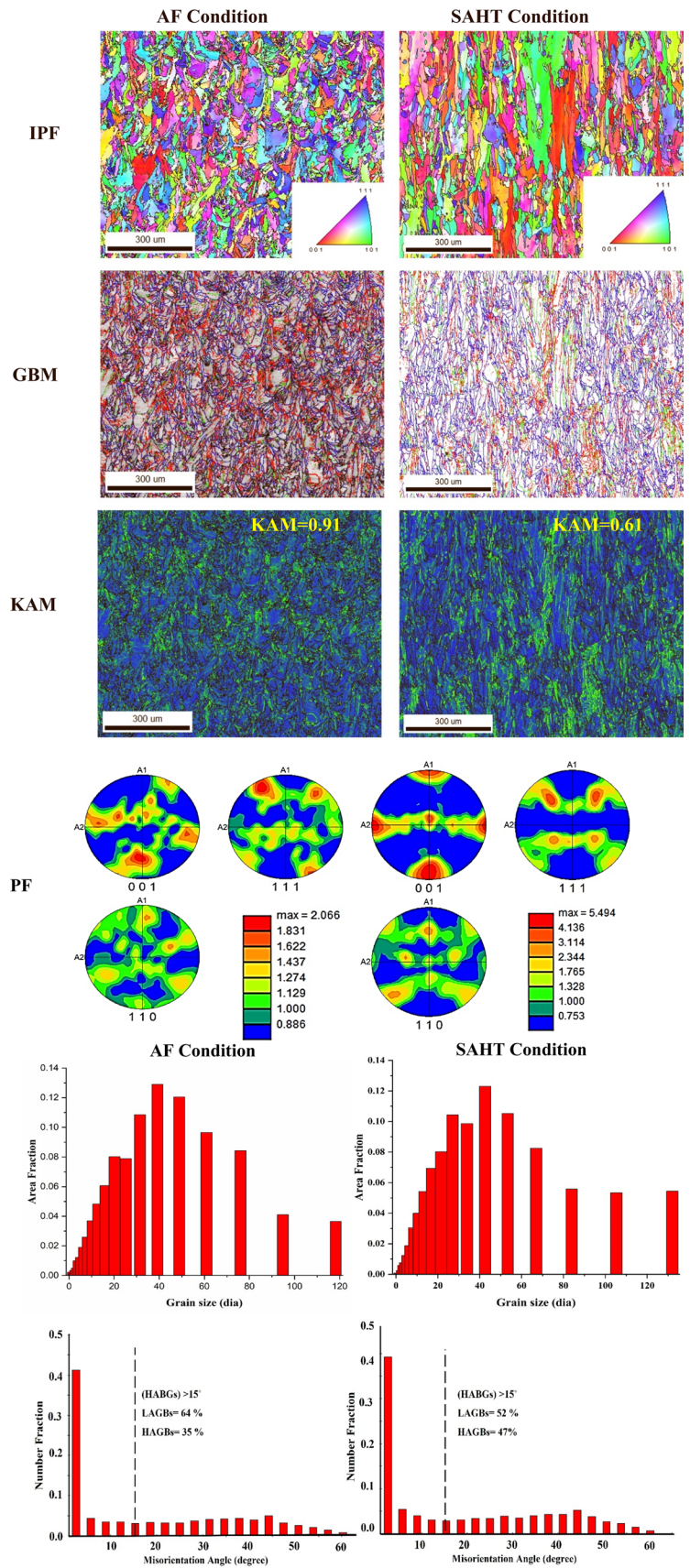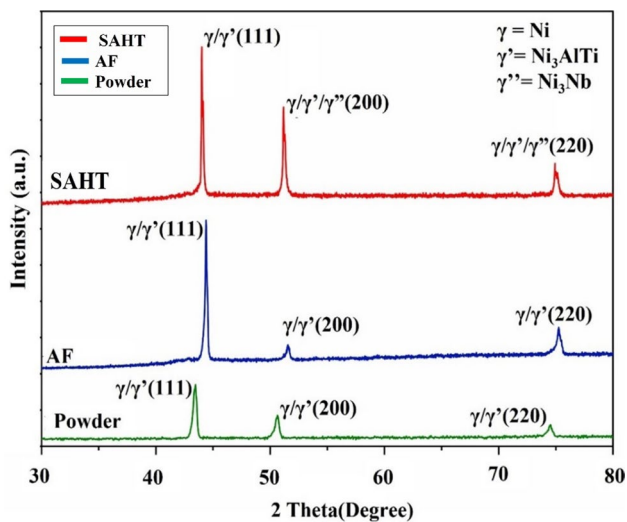
Fig. 16 XRD pattern results of L-PBF IN718 in AF and SAHT condition
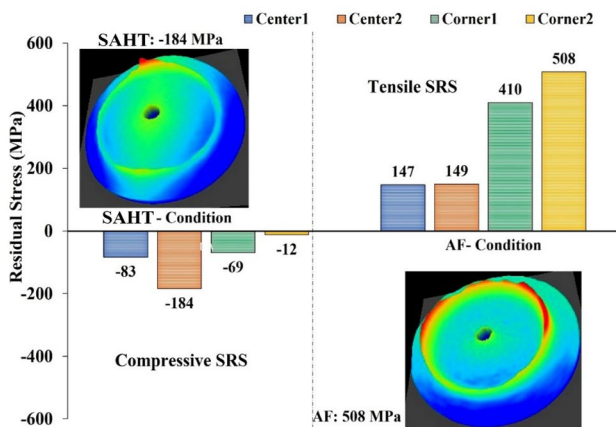
Fig. 17 SRS distribution of L-PBF IN718 in AF and SAHT condition

small crystalline structure with nano-sized lave particles is hard to detect.

### 3.3 Residual stress (RS) analysis

Figure 17 shows that the SRS is distributed across the top surfaces under the AF and SAHT conditions. When the top layer attempts to contract, it is often impeded by the layers underneath it, resulting in the emergence of TSRS. AF samples revealed the tensile nature of SRS on their upper surface. The presence of TG in both the interlayer and intralayer is the primary explanation for SRS nucleation during the L-PBF process. The degree of SRS was also discovered to vary within the uppermost layer. Within the final printed top layer, the magnitude of SRS varied from 76 to 149 MPa in the mid-surface areas and from 410 to 625 MPa in the

corner-surface regions. When comparing the corner surface area to the mid-surface region, the average magnitude of SRS was 77% larger. The fundamental reason for this is the extreme temperature difference between the powder bed and the printed layers above it. Powder particles have a thermal conductivity of 1.67 W/mK, whereas the solidified material has a conductivity of 11.9 W/mK [45]. As a consequence, this tendency causes more TSRSs to cluster at the edges than in the central region. In addition, SRS built up around sharp edges because to the shape of the parts. Wu As et al. [46] reported that the abrupt change in part geometry has a significant influence on the SRS development. The final printed top layer of the SAHT samples showed surface CSRS variations in magnitude from −83 to −184 MPa in the central surface area and from −12 to −69 MPa in the corner surface regions. This is mainly due to the fact that the hexagonal Laves phase with a greater lattice spacing of 0.487 nm in the AF sample was replaced by BCT γ'' with a reduced lattice spacing of 0.284 nm, FCC γ' with 0.322 nm resulting in CSRS in the basic γ matrix. On the other hand, the orthorhombic δ phase had a lattice spacing of 0.5114 nm, larger than the basic γ matrix, which caused a small rise in SRS magnitude [42]. Compared to the larger lattice spacing δ phase, the smaller lattice spacing γ'' phase was more after SAHT and resulted in CSRS. Based on the crystal orientation, the diffracted X-rays form a cone-shaped Debye ring with diverse peaks structure in the samples. The Debye ring and diffracted peaks of both AF and SAHT samples are represented in Fig. 18. From the figure, it was observed that the Debye ring for HT representing CSRS was found to slide towards the right from the left side of the AF samples generated Debye ring. The diffracted peaks were observed to be broadened after SAHT due to the decrease in interplanar d spacing, which represented the CSRS. The typical stress–strain plot developed from the cosα method was observed to be increased for SAHT samples, confirms that the even distribution of SRS and grains structure over AF condition. Further, the diffraction angle of (full width half maximum) FWHM angle was found to be increased after SAHT, which helps to confirm the grain refinements. Further, compared to AF samples, SAHT induces recrystallization associated with the conversion of LAGBS to HAGBS, resulting in an even distribution of CRS magnitude.

3.4 Mechanical properties analysis

Figure 19 presents a comparison of the tensile performance shown by AF and SAHT samples. Following the application of the SAHT process, there was a notable enhancement in both the yield and ultimate tensile strength, with increases of 26.44% and 44.74% observed, respectively. Conversely, there was a decrease of 36.19% seen in ductility. The AF and SAHT samples of L-PBF IN718 exhibited

Fig. 18 Debye ring; diffraction peak; FWHM versus α plots; normal strain plots of AF and SAHT IN718 superalloy
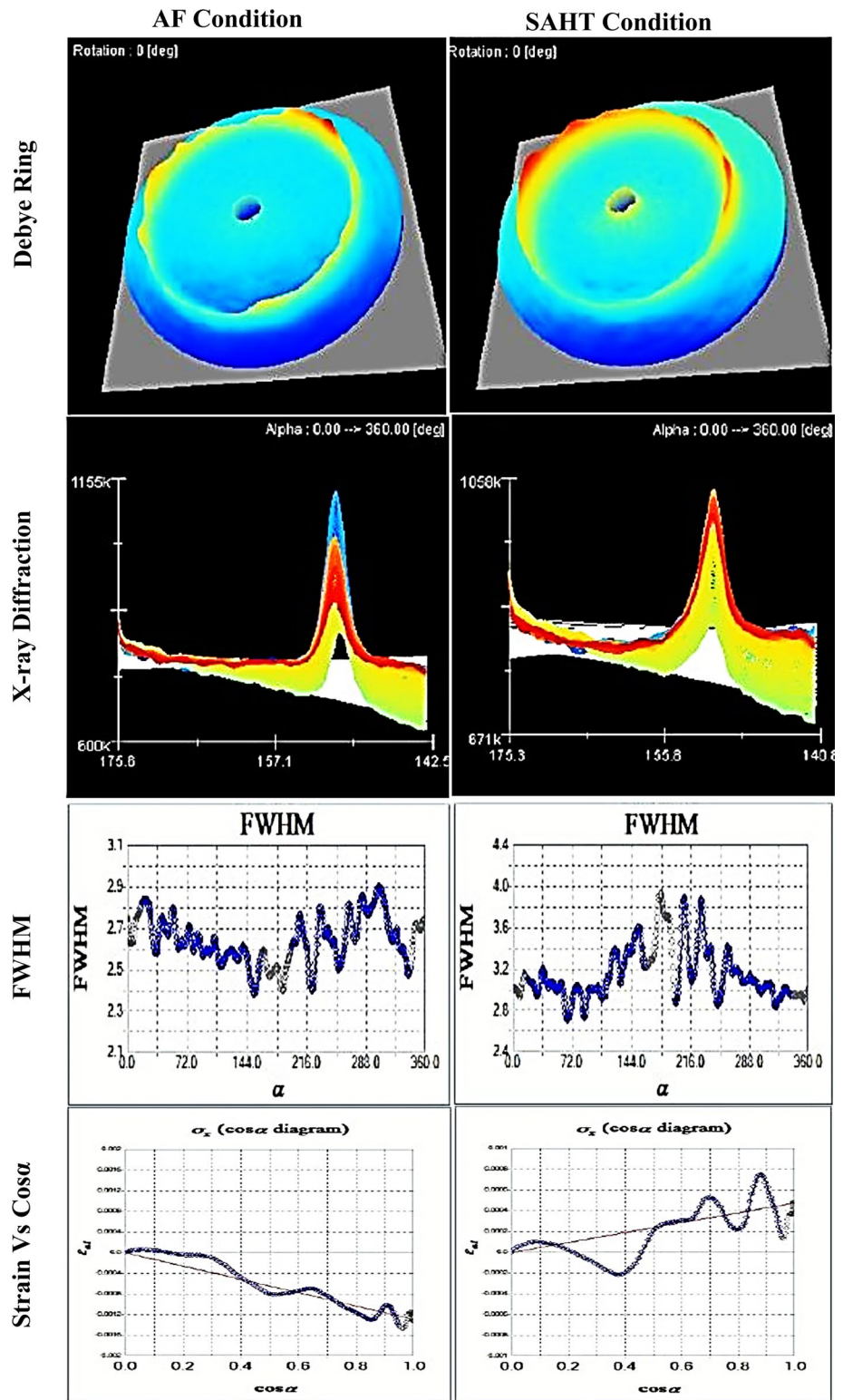
mechanical qualities that significantly above the minimum required thresholds [47]. The ageing treatment has a crucial role in facilitating the precipitation of strengthening phases (γ' and γ''). The enhancement in tensile strength seen throughout the process of solution annealing and ageing has been attributed to the formation of precipitates consisting of the strengthening phases γ' and γ''. SAHT sample's strength was enhanced by the significant strengthening γ'' phase, that precipitated inside the matrix, as well as the presence of the δ phase at the grain boundary. The primary cause of a
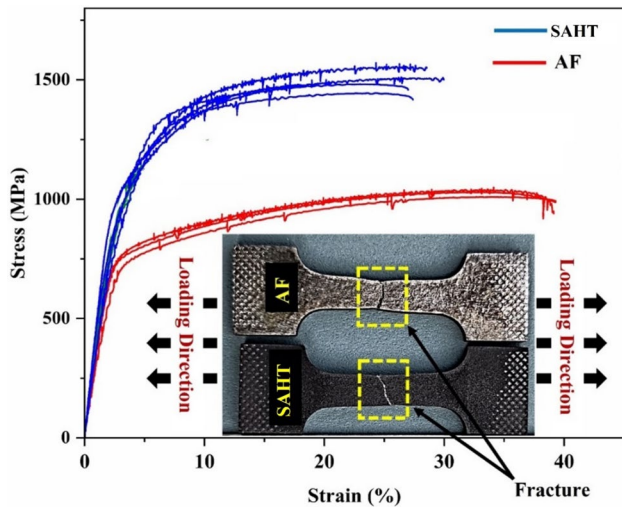
Fig. 19 Stress–strain curve of AF and SAHT of L-PBF fabricated IN718

notable decrease in ductility in SAHT may be attributed to the formation of needle-shaped δ phase at the grain boundary. The low ductility of SAHT samples may be attributed to the dislocation pinning effect generated by the presence of γ' and γ'' phases, as well as the restriction of dislocation mobility by the needle-shaped δ phase at the grain boundary [13]. Figure 20 displays the fracture surface morphologies of both the AF and SAHT samples. Ductile fracture was seen in both samples, as shown by the existence of dimple networks on the morphologies of the broken surfaces. The fracture surface of AF samples had a cluster of additional dimples, whereas SAHT samples demonstrated the existence of dimples that were more uneven and greater in size.

4 Conclusion

The impact of the step-by-step post-SAHT on the microstructure, texture, SRS, and mechanical characteristics of IN718 manufactured by LPBF for aerospace applications has been examined in the current research. The key conclusions could potentially be given out as follows:
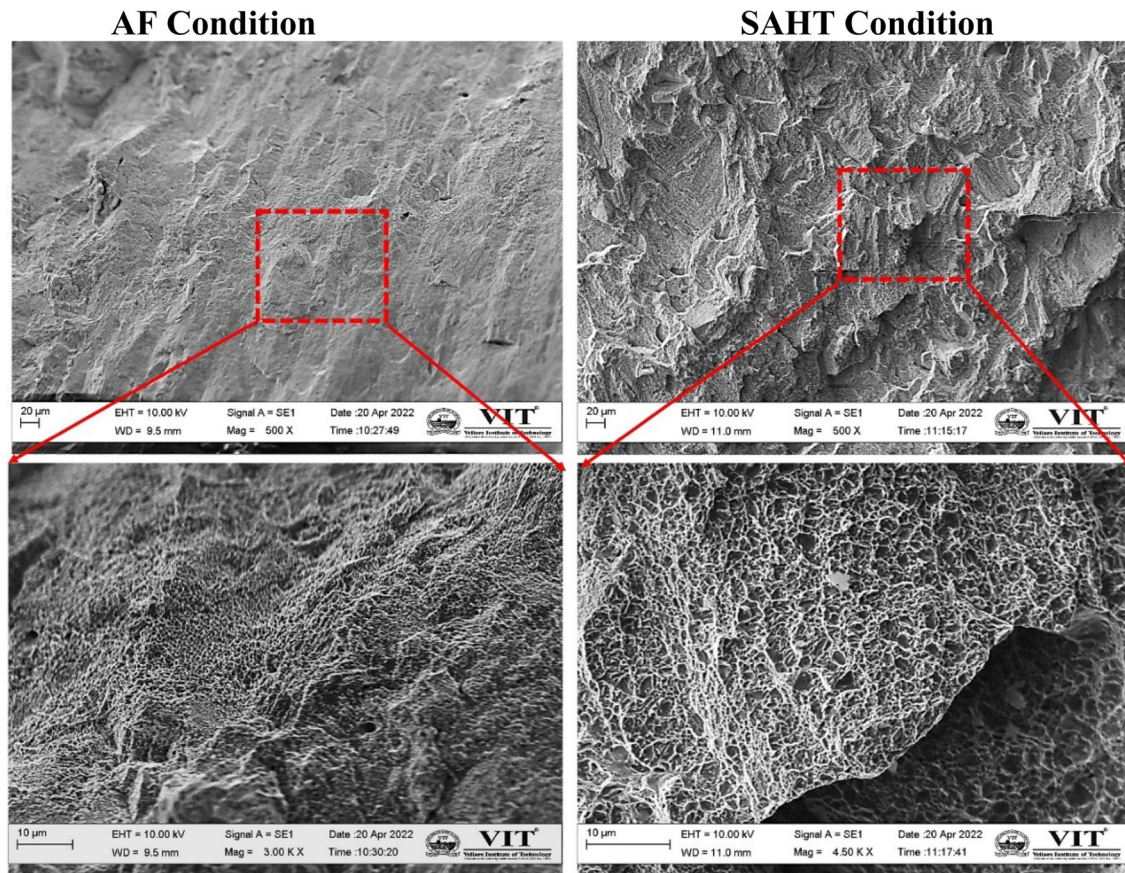
Fig. 20 Fracture surface of L-PBF IN718: AF condition and SAHT condition

- The microstructure of IN718 in after L-PBF displayed arc-shaped boundaries of the melt pools and a columnar dendritic structure. Additionally, Laves phases were seen in the interdendritic areas along the direction of fabrication. The microstructure of IN718 saw considerable alterations during the process of SAHT. The use of SAHT caused modifications in the microstructure of the AF material by a process of recrystallization. This resulted in the formation of a uniform distribution of equiaxed grains, with the elimination of melt pool borders and Laves phases. The microstructure of the SAHT sample exhibited the homogeneous precipitation of γ' and γ'' strengthening phases inside the γ matrix, accompanied by the presence of δ phases and brittle Laves phases at the grain boundaries.

- SAHT caused increase in grain size from 41.56 to 44.80 μm, the LAGBs were converted to HAGBs, and a decrease in KAM values. In addition, the columnar texture in AF conditions was converted to cubical texture in <100> and <010> direction in (001) plane which confirms the recrystallization and homogenization after SAHT.

- TSRS were clearly visible on the AF samples outermost top surface. It was also shown that there was a 77% increase in the percentage variance in SRS magnitude within the top layer in the corner locations. The phase transformation led to the conversion of TSRS in AF samples into CSRS after SAHT. The SAHT effectively induced even distribution of CRS magnitude due to recrystallization at higher temperature solution annealing and ageing process.

- AF IN718 alloy demonstrated reduced strength accompanied by increased elongation as a result of the precipitation of Laves phases. The highest ductility was observed in AF condition due to the presence of LAGBs and the absence of strengthening γ'' phases. The mechanical properties were effectively improved after SAHT compared to AF conditions. Following SAHT, the yield and ultimate tensile strength exhibited an increase of 26.44% and 44.74%, respectively. Conversely, there was a decrease in the percentage of elongation to 36.19%. The observed behaviour may be primarily attributed to the precipitation of reinforcing γ' and γ'' phases, as well as the hindrance of dislocation movement caused by the needle-shaped δ phase that precipitated along the grain boundary.

Declarations

References

1. Srinivasan D, Ananth K (2022) Recent advances in alloy development for metal additive manufacturing in gas turbine/aerospace applications: a review. J Indian Inst Sci 102:311–349. https://doi.org/10.1007/s41745-022-00290-4

2. Lee J-Y, An J, Chua CK (2017) Fundamentals and applications of 3D printing for novel materials. Appl Mater Today 7:120–133. https://doi.org/10.1016/j.apmt.2017.02.004

3. Sunay N, Kaya M, Yılmaz MS, Kaynak Y (2023) Effects of heat treatment on surface integrity and wear performance of Inconel 718 alloy fabricated by laser powder bed fusion process additive manufacturing under different laser power and scanning speed parameters. J Braz Soc Mech Sci Eng. https://doi.org/10.1007/s40430-023-04298-4

4. Patel S, deBarbadillo J, Coryell S (2018) Superalloy 718: Evolution of the alloy from high to low temperature application. In: Proceedings of the 9th international symposium on superalloy 718 and derivatives: energy, aerospace, and industrial applications. Springer, Cham, pp 23–49

5. Bhuvanesh Kumar M, Sathiya P, Senthil SM (2023) A critical review of wire arc additive manufacturing of nickel-based alloys: principles, process parameters, microstructure, mechanical properties, heat treatment effects, and defects. J Braz Soc Mech Sci Eng. https://doi.org/10.1007/s40430-023-04077-1

6. Blakey-Milner B, Gradl P, Snedden G et al (2021) Metal additive manufacturing in aerospace: a review. Mater Des 209:110008. https://doi.org/10.1016/j.matdes.2021.110008

7. Marques A, Guimarães B, Bartolomeu F et al (2023) Multi-material Inconel 718 – Aluminium parts targeting aerospace applications: a suitable combination of low-weight and thermal properties. Opt Laser Technol 158:108913. https://doi.org/10.1016/j.optlastec.2022.108913

8. Kaur I, Aider Y, Nithyanandam K, Singh P (2022) Thermal-hydraulic performance of additively manufactured lattices for gas turbine blade trailing edge cooling. Appl Therm Eng 211:118461. https://doi.org/10.1016/j.applthermaleng.2022.118461

9. Paulonis DF, Schirra JJ (2001) Alloy 718 at Pratt and Whitney: historical perspective and future challenges. In: Superalloys 718, 625, 706 and various derivatives (2001), TMS

10. Sonar T, Balasubramanian V, Malarvizhi S et al (2021) Influence of magnetically constricted arc traverse speed (MCATS) on tensile properties and microstructural characteristics of welded Inconel 718 alloy sheets. Def Technol 17:1395–1413. https://doi.org/10.1016/j.dt.2020.07.009

11. Sanjeeviprakash K, Kannan AR, Shanmugam NS (2023) Additive manufacturing of metal-based functionally graded materials: overview, recent advancements and challenges. J Braz Soc Mech Sci Eng. https://doi.org/10.1007/s40430-023-04174-1

12. Gisario A, Kazarian M, Martina F, Mehrpouya M (2019) Metal additive manufacturing in the commercial aviation industry: a review. J Manuf Syst 53:124–149. https://doi.org/10.1016/j.jmsy.2019.08.005

13. Fayed EM, Saadati M, Shahriari D et al (2021) Effect of homogenization and solution treatments time on the elevated-temperature mechanical behavior of Inconel 718 fabricated by laser

powder bed fusion. Sci Rep 11:2020. https://doi.org/10.1038/s41598-021-81618-5

14. Zhang D, Feng Z, Wang C et al (2018) Comparison of microstructures and mechanical properties of Inconel 718 alloy processed by selective laser melting and casting. Mater Sci Eng A Struct Mater 724:357–367. https://doi.org/10.1016/j.msea.2018.03.073

15. Wang X, Gong X, Chou K (2017) Review on powder-bed laser additive manufacturing of Inconel 718 parts. Proc Inst Mech Eng Pt B: J Eng Manuf 231:1890–1903. https://doi.org/10.1177/0954405415619883

16. Yang G, Liu B, Li L et al (2022) In situ measurement and numerical simulation on deformation in laser depositing Inconel 718. J Braz Soc Mech Sci Eng. https://doi.org/10.1007/s40430-022-03822-2

17. Cheng L, Liang X, Bai J et al (2019) On utilizing topology optimization to design support structure to prevent residual stress induced build failure in laser powder bed metal additive manufacturing. Addit Manuf 27:290–304. https://doi.org/10.1016/j.addma.2019.03.001

18. Akram J, Kalvala PR, Jindal V, Misra M (2018) Evaluating location specific strain rates, temperatures, and accumulated strains in friction welds through microstructure modeling. Def Technol 14:83–92. https://doi.org/10.1016/j.dt.2017.11.002

19. Xu X-Y, Ma X-D, Wang H et al (2019) Characterization of residual stresses and microstructural features in an Inconel 718 forged compressor disc. Trans Nonferrous Met Soc China 29:569–578. https://doi.org/10.1016/s1003-6326(19)64965-4

20. Patterson AE, Messimer SL, Farrington PA (2017) Overhanging features and the SLM/DMLS residual stresses problem: review and future research need. Technologies 5:15. https://doi.org/10.3390/technologies5020015

21. Gokcekaya O, Ishimoto T, Hibino S et al (2021) Unique crystallographic texture formation in Inconel 718 by laser powder bed fusion and its effect on mechanical anisotropy. Acta Mater 212:116876. https://doi.org/10.1016/j.actamat.2021.116876

22. Ghorbanpour S, Sahu S, Deshmukh K et al (2021) Effect of microstructure induced anisotropy on fatigue behaviour of functionally graded Inconel 718 fabricated by additive manufacturing. Mater Charact 179:111350. https://doi.org/10.1016/j.matchar.2021.111350

23. Al-Maharma AY, Patil SP, Markert B (2020) Effects of porosity on the mechanical properties of additively manufactured components: a critical review. Mater Res Express 7:122001. https://doi.org/10.1088/2053-1591/abcc5d

24. du Plessis A (2019) Effects of process parameters on porosity in laser powder bed fusion revealed by X-ray tomography. Addit Manuf 30:100871. https://doi.org/10.1016/j.addma.2019.100871

25. Mohd Yusuf S, Cutler S, Gao N (2019) Review: the impact of metal additive manufacturing on the aerospace industry. Metals 9:1286. https://doi.org/10.3390/met9121286

26. Sangid MD, Book TA, Naragani D et al (2018) Role of heat treatment and build orientation in the microstructure sensitive deformation characteristics of IN718 produced via SLM additive manufacturing. Addit Manuf 22:479–496. https://doi.org/10.1016/j.addma.2018.04.032

27. Kim SY, Luzin V, Sesso ML et al (2020) The effect of low temperature range heat treatment on the residual stress of cold gas dynamic sprayed inconel 718 coatings via neutron diffraction. J Therm Spray Technol 29:1477–1497. https://doi.org/10.1007/s11666-020-01080-z

28. Barros R, Silva FJG, Gouveia RM et al (2019) Laser powder bed fusion of inconel 718: residual stress analysis before and after heat treatment. Metals 9:1290. https://doi.org/10.3390/met9121290

29. Zhang H, Li C, Liu Y et al (2017) Effect of hot deformation on γ'' and δ phase precipitation of Inconel 718 alloy during deformation and isothermal treatment. J Alloys Compd 716:65–72. https://doi.org/10.1016/j.jallcom.2017.05.042

30. Chlebus E, Gruber K, Kuźnicka B et al (2015) Effect of heat treatment on the microstructure and mechanical properties of Inconel 718 processed by selective laser melting. Mater Sci Eng A Struct Mater 639:647–655. https://doi.org/10.1016/j.msea.2015.05.035

31. Slama C, Abdellaoui M (2000) Structural characterization of the aged Inconel 718. J Alloys Compd 306:277–284. https://doi.org/10.1016/s0925-8388(00)00789-1

32. Azadian S, Wei L-Y, Warren R (2004) Delta phase precipitation in Inconel 718. Mater Charact 53:7–16. https://doi.org/10.1016/j.matchar.2004.07.004

33. Tucho WM, Hansen V (2021) Studies of post-fabrication heat treatment of L-PBF-Inconel 718: effects of hold time on microstructure, annealing twins, and hardness. Metals 11:266. https://doi.org/10.3390/met11020266

34. Dinda GP, Dasgupta AK, Mazumder J (2009) Laser aided direct metal deposition of Inconel 625 superalloy: microstructural evolution and thermal stability. Mater Sci Eng A Struct Mater 509:98–104. https://doi.org/10.1016/j.msea.2009.01.009

35. Calandri M, Yin S, Aldwell B et al (2019) Texture and microstructural features at different length scales in Inconel 718 produced by selective laser melting. Materials 12:1293. https://doi.org/10.3390/ma12081293

36. Sochalski-Kolbus LM, Payzant EA, Cornwell PA et al (2015) Comparison of residual stresses in inconel 718 simple parts made by electron beam melting and direct laser metal sintering. Metall Mater Trans A 46:1419–1432. https://doi.org/10.1007/s11661-014-2722-2

37. Gruber K, Dziedzic R, Kuźnicka B et al (2021) Impact of high temperature stress relieving on final properties of Inconel 718 processed by laser powder bed fusion. Mater Sci Eng A Struct Mater 813:141111. https://doi.org/10.1016/j.msea.2021.141111

38. Chen Y, Cernatescu I, Venkatesh V et al (2023) On the residual stress relaxation in Inconel 718 superalloys at high temperature by real-time neutron diffraction. Mater Des 232:112135. https://doi.org/10.1016/j.matdes.2023.112135

39. Liu L, Wang D, Yang Y et al (2023) Effect of scanning strategies on the microstructure and mechanical properties of Inconel 718 alloy fabricated by laser powder bed fusion. Adv Eng Mater. https://doi.org/10.1002/adem.202200492

40. Xiao H, Liu X, Xiao W et al (2022) Influence of molten-pool cooling rate on solidification structure and mechanical property of laser additive manufactured Inconel 718. J Mater Res Technol 19:4404–4416. https://doi.org/10.1016/j.jmrt.2022.06.162

41. Wang G, Ouyang H, Fan C et al (2020) The origin of high-density dislocations in additively manufactured metals. Mater Res Lett 8:283–290. https://doi.org/10.1080/21663831.2020.1751739

42. Mahadevan S, Nalawade S, Singh JB et al (2010) Evolution of δ phase microstructure in alloy 718. In: Ott EA, Groh JR, Banik A, Dempster I, Gabb TP, Helmink R, Liu X, Mitchell A, Sjöberg GP, Wusatowska-Sarnek A (eds) Superalloy 718 and derivatives. Wiley, New York, pp 737–750

43. Idell Y, Levine LE, Allen AJ et al (2016) Unexpected δ-phase formation in additive-manufactured Ni-based superalloy. JOM 68:950–959. https://doi.org/10.1007/s11837-015-1772-2

44. Park JH, Bang GB, Lee K-A et al (2021) Effect on microstructural and mechanical properties of Inconel 718 superalloy fabricated by selective laser melting with rescanning by low energy density. J Mater Res Technol 10:785–796. https://doi.org/10.1016/j.jmrt.2020.12.053

45. An K, Yuan L, Dial L et al (2017) Neutron residual stress measurement and numerical modeling in a curved thin-walled structure by laser powder bed fusion additive manufacturing. Mater Des 135:122–132. https://doi.org/10.1016/j.matdes.2017.09.018

46. Wu AS, Brown DW, Kumar M et al (2014) An experimental investigation into additive manufacturing-induced residual stresses in 316L stainless steel. Metall Mater Trans A 45:6260–6270. https://doi.org/10.1007/s11661-014-2549-x

47. Sadeghi E, Karimi P, Esmaeilizadeh R et al (2023) A state-of-the-art review on fatigue performance of powder bed fusion-built alloy 718. Prog Mater Sci 133:101066. https://doi.org/10.1016/j.pmatsci.2022.101066

Authors and Affiliations

Praveenkumar Vijayakumar[1] · S. Raja[2] · Maher Ali Rusho[3] · G. L. Balaji[4]

✉ Praveenkumar Vijayakumar
praveenkv@am.amrita.edu; shasha.praveen@gmail.com

S. Raja
engineerraja@yahoo.com; sraja@citchennai.net

Maher Ali Rusho
maher.rusho@colorado.edu

G. L. Balaji
balajivinayaka84@gmail.com

[1] Department of Mechanical Engineering, Amrita Vishwa Vidyapeetham, Amritapuri, Kollam, Kerala 690525, India

[2] Center for Sustainable Materials and Surface Metamorphosis, Chennai Institute of Technology, Chennai 600069, India

[3] Specialized Program Grad Student, Lockheed Martin Performance-Based Master of Engineering in Engineering Management (ME-EM) Degree Program, University of Colorado Boulder, Boulder, CO 80309, USA

[4] Department of Research and Innovation, Saveetha School of Engineering, SIMATS, Chennai, Tamil Nadu 602105, India